Journal of Materials Chemistry A

ROYAL SOCIETY OF CHEMISTRY

PAPER

Cite this: *J. Mater. Chem. A*, 2020, **8**, 13364

Tunable LiCl@UiO-66 composites for water sorption-based heat transformation applications†

Yangyang Sun, [a] Alex Spieß,[a] Christian Jansen, [a] Alexander Nuhnen,[a] Serkan Gökpinar,[a] Raphael Wiedey,[b] Sebastian-Johannes Ernst [c] and Christoph Janiak *[a]

Received 27th March 2020
Accepted 12th June 2020

DOI: 10.1039/d0ta03442h

rsc.li/materials-a

Porous composite materials are potential candidates for water-based adsorptive heat transformation (AHT) applications. Here, a solid adsorbent LiCl@UiO-66 as a 'composite salt inside porous matrix' (CSPM) has been prepared by incorporating hygroscopic lithium chloride into a microporous metal–organic framework (MOF) UiO-66 as a host matrix through the wet impregnation method. In our wet impregnation we did not let the excess salt solution dry to prevent salt precipitation on the matrix surface. This yielded a true salt@MOF composite with no deliquescence of LiCl and strongly enhanced the water adsorption capacity of UiO-66 through the salt content. At $p/p_0 = 0.1$ the water vapor sorption isotherms show a hydration state of LiCl inside the MOF of LiCl·2–4H_2O which is much higher than for neat LiCl with 0.5H_2O, due to the dispersion of a small particle size inside the matrix. LiCl@UiO-66 with a 30 wt% LiCl content (LiCl@UiO-66_30) has a 3 to 8 times higher water uptake over neat UiO-66 (depending on relative pressure) and could reach a volumetric and gravimetric water uptake of over 2.15 g g^{-1} at $p/p_0 = 0.9$, which outperforms the so far known UiO-66-based composites. Cycling tests confirmed the hydrothermal stability of the LiCl@UiO-66 composites. Kinetic evaluation of the gravimetric water uptake (at 90% relative humidity) over time yielded rate coefficients up to 2.0(1) × 10^{-4} s^{-1} which is slower than that in neat UiO-66 (6.7(6) × 10^{-4} s^{-1}) but faster than that for salt@silica gel composites. The coefficient of performance for the heat pumping mode (at $T_{des}/T_{ads}/T_{evap}$ set to 90/40/10 °C) of 1.64 for LiCl@UiO-66_30 exceeds those of other MOFs, salt@MOF or salt@silica gel composites. For thermal battery applications the heat storage capacity (C_{HS}) for LiCl@UiO-66_30 is 900 kJ kg^{-1} (=0.25 kW h kg^{-1}), which can reach the Department of Energy (DOE) value of 2.5 kW h/35 kg with just 10 kg of material and outperforms $CaCl_2$@UiO-66_38 with a C_{HS} value of 367 kJ kg^{-1}.

Introduction

Adsorptive heat transformation (AHT) systems have demonstrated the possibility to run air conditioners with lower electricity consumption than compressor systems by operating on low thermal energy sources such as industrial waste heat and solar energy for regeneration and driving energy.[1–4] AHT is based on cycling adsorption and desorption of a working fluid in a highly porous substrate (Fig. S1, ESI†). AHT includes different branches such as adsorption heat pumps (AHPs), adsorption chillers and heat storage. Different vapors can be used as the working fluid, like methanol, ethanol and water. Water is preferred for AHT, because of its high evaporation enthalpy, ready availability and environmentally friendly features.

To date, many kinds of porous materials have been investigated for adsorptive heat transformation (AHT), including silica gels,[5] activated carbon,[6,7] zeolites,[8] aluminophosphates[9,10] and more recently metal–organic frameworks (MOFs).[11–16] Two recent studies of MOFs for AHT include using a new MOF framework CAU-23 with ultra-low regeneration temperature for adsorption chillers[17] and an easy hydrophilicity tuning of Al-Based MOFs through a solid-solution mixed-linker strategy.[18] MOFs can be designed or functionalized by post-synthetic modification to increase their water uptake capacity and adjust the relative vapor pressure region.[19–23] Although some investigations of MOFs have been made in AHT, disadvantageous aspects, such as low adsorption capacity, are still to be tackled in real applications.

[a]*Institut für Anorganische Chemie und Strukturchemie, Heinrich-Heine-Universität Düsseldorf, 40204 Düsseldorf, Germany. E-mail: janiak@hhu.de*

[b]*Institut für Pharmazeutische Technologie und Biopharmazie, Heinrich-Heine-Universität Düsseldorf, 40204 Düsseldorf, Germany*

[c]*Fraunhofer Institute for Solar Energy Systems (ISE), Heidenhofstr. 2, 79110 Freiburg, Germany*

† Electronic supplementary information (ESI) available: Schemes for AHT, water sorption in CSPMs, and details of AAS; SEM/EDX elemental mapping; TGA and defect calculation of UiO-66; PXRD recycled UiO-66; full water sorption isotherms; images of CSPM; gravimetric multi-cycle water sorption graphs; kinetic fits of water sorption isotherms and COP calculation. See DOI: 10.1039/d0ta03442h

A 'composite salt inside porous matrix' (CSPM) combines a porous material as a matrix and an inorganic salt as an active ingredient.[24] The inorganic salt is intended to improve the water sorption capacity of the porous material, and the matrix of the porous material could avoid the drawbacks of inorganic salts in an AHT process such as deliquescence and intumescence (swelling up) (deliquescence is the absorption of moisture by a substance until it dissolves in the absorbed water to yield a solution).

Mechanistically water sorption on a CSPM is considered to occur by water adsorption on the host matrix, inducing the chemical reaction between water and salt, resulting in the formation of crystalline hydrates, and eventually water *ab*sorption by the aqueous salt solution in the pores (Fig. S2, ESI†). The host matrix provides for efficient transfer of the heat of hydration and disperses the salt reagent, which greatly enhances the reaction kinetics. The vapor–solid reaction is much faster for a dispersed salt inside the host than for a bulk salt, so that the rate of the sorption process is only controlled by inter- or intra-particle diffusion. Consequently, the water sorption by a composite is not a linear combination of that of the host matrix and salt.[24–27] Therefore, salt@MOF composites should combine the merits of the salt and the pore features of the MOF. The typical active salts for CSPMs are halides, sulfates, and nitrates of alkali and alkali-earth metals.[28] Moreover, a porous material with an already higher water uptake capacity under low relative pressure (p/p_0 below 0.3) is preferred for AHTs.

Up to now, only a few MOF-based CSPMs have been reported. Garzón-Tovar *et al.* developed a UiO-66-based CSPM adsorbent with 38 wt% $CaCl_2$ for thermal batteries and 53 wt% $CaCl_2$ for refrigerators using a spray-drying continuous flow method.[29] Permyakova *et al.* analyzed six water-stable MOFs containing $CaCl_2$, prepared by soaking MOFs in an inorganic salt solution. It was demonstrated that mesoporous and amphiphilic robust MOFs could achieve a higher salt encapsulation rate. The higher loading lifts and energy storage densities of MIL-100(Fe) with 46 wt% $CaCl_2$ and MIL-101(Cr) with 62 wt% $CaCl_2$ composite sorbents were suggested for seasonal heat storage.[30] Tan *et al.* synthesized composites salt@MIL-101(Cr) whose salt content was up to 60 wt% $CaCl_2$ and 42 wt% LiCl when the salt solution concentration was 30% $CaCl_2$ and 20% LiCl through incipient wetness impregnation. For the 60 wt% CSPM deliquescence was observed, but the composites with 53 wt% $CaCl_2$ and 36 wt% LiCl exhibited low desorption activation energy, fast sorption rates and high adsorption in low humidity compared to neat MIL-101(Cr).[31] Xu *et al.* reported LiCl@MIL-101(Cr) composites through adding a specified quantity of LiCl into a well-dispersed MIL-101(Cr) aqueous suspension (5 mg mL^{-1}) for sorption-based atmospheric water harvesting (AWH) in arid climates. LiCl@MIL-101(Cr) composites have a high-water sorption performance of 0.77 g g^{-1} under arid working conditions (30% RH at 30 °C) and an AWH device based on this composite adsorbent can utilize natural sunlight without requiring additional energy.[23] All these efforts showed that the water vapor uptake of MOFs could be improved after incorporating salt into the parent adsorbent.

Herein, we have explored the influence of three different weight fractions of LiCl on the sorption properties of UiO-66-based novel LiCl@UiO-66 CSPMs. Extensive thermodynamic and kinetic water adsorption studies were carried out on UiO-66-based CSPMs, which show no deliquescence but a higher water adsorption capacity than neat UiO-66. We selected UiO-66 as the porous matrix because of its exceptional chemical and thermal stability.[32] LiCl was chosen due to its known high hydrophilicity.[33]

Experimental

Materials and instrumentation

The chemicals used were obtained from commercial sources. Zirconium(IV) chloride ($ZrCl_4$, 98%) was bought from Alfa Aesar, 1,4-benzenedicarboxylic acid (H_2BDC, >99%) from Acros Organics, *N*,*N*-dimethylformamide (DMF, 99.5%) from Fisher Chemicals, and lithium chloride anhydrous was purchased from Fischer Scientific. No further purification was carried out. The water used was Millipore deionized water.

Powder X-ray diffractometry (PXRD) was performed at room temperature on a Bruker D2 Phaser powder diffractometer equipped with a flat silicon, low background sample holder using Cu-Ka radiation ($\lambda = 1.5418$ Å) in the range of $5° < 2\theta < 50°$ with a scanning rate of 0.0125° s^{-1} (300 W, 30 kV, 10 mA). The analyses of the diffractograms were carried out with "Match! 3.5.3.109" software.

SEM images were acquired on a Jeol JSM-6510LV QSEM Advanced electron microscope (Jeol, Akishima, Japan) with a LaB6 cathode at 5–20 keV. The microscope was equipped with an Xflash 410 (Bruker, Billerica, US) silicon drift detector and Bruker ESPRIT software for EDX analysis.

The adsorption–desorption isotherms of nitrogen were measured at 77 K using an Autosorb-6 from Quantachrome and evaluated with AsiQwin V3 software. For activation, the sample was degassed in a vacuum of 5×10^{-2} mbar at 150 °C for 12 h. The Brunauer–Emmett–Teller (BET) surface areas were calculated in the p/p_0 range of 0.01–0.05. Total pore volumes were calculated from nitrogen adsorption isotherms at $p/p_0 = 0.90$. Nitrogen sorption isotherms were also recorded on a Micrometrics ASAP 2020 in order to obtain the pore size distribution which was calculated using the NDFT method at 77 K for "N_2 on cylindrical pores".

Flame atomic absorption spectroscopy (AAS) was performed on a PerkinElmer PinAAcle 900T spectrometer equipped with a single element lithium hollow cathode lamp and using an acetylene/air flame. The wavelength of Li is 670.78 nm. The slit width in the spectrometer was 0.2 nm.

A Varian 715-ES ICP-optical emission spectrometer was used. Approximately 5 mg of the sample was mixed with 8 mL of aqua regia and 2 mL of hydrofluoric acid. The digestion was performed in a microwave-assisted sample preparation system "Multiwave PRO" from Anton Paar at ~220 °C and ~50 bar pressure. The digested solution was filled up to 100 mL and measured by ICP-OES. The data analysis was performed on Varian 715-ES software "ICP Expert".

Water vapor sorption multi-cycle tests of the composites were carried out with a gravimetric SPS11-10μ water sorption

analyzer from proUmid, Germany. The mass of the sample was recorded every 10 minutes by using an electronic balance with an accuracy of ±10 μg. For each sample, the mass change at different sorption times was calculated as mass change at equilibrium related to the lowest net weight in %. Cycles between relative humidity levels of 90% and 0% were carried out under a maximum equilibration time of 3 hours per climate cycle. The minimal mass of each sample was 50 mg. The adsorption kinetics curve was acquired at 20 °C and at a set target relative humidity of 90%, which took around one hour in the chamber. Another 40 cycles were performed under a relative humidity of 80% and 20% with a maximal equilibration time per climate cycle of 2 h. The general equilibrium condition was 0.01% per 15 minutes.

Volumetric water vapor sorption isotherms were recorded on a Quantachrome VSTAR vapor sorption analyzer at 293 K. For activation, the sample was evacuated on a FloVac®Degasser at 150 °C for 16 h. The volumetric water sorption measurement was performed under the "slowest" possible conditions, that is, the maximum possible time provided by the setting parameters before the measurement advanced to the next data point. The equilibrium settings for volumetric measurement under 'pressure points mode' were 'Equilibrium points number: 10'; 'Equilibrium points interval time (s): 90 to 180'; 'Sorption rate limit (Torr min^{-1}): 0.001 to 0.01'. From repeated and reproducible volumetric water vapor sorption isotherms the variance of the water uptake values is around 5%.

Thermogravimetric analysis (TGA) was done with a Netzsch TG 209 F3 Tarsus in the range from 25 to 600 °C, equipped with an Al_2O_3-crucible and applying a heating rate of 5 K min^{-1} under air atmosphere.

Synthesis of UiO-66

UiO-66, $[Zr_6(\mu_3\text{-}O)(\mu_3\text{-}OH)_4(BDC)_6]$ (BDC = benzene-1,4-dicarboxylate, terephthalate), was synthesized using a slightly modified procedure of Lillerud *et al.*,[34] by decreasing the amount of *N*,*N*-dimethylformamide, DMF. The molar ratio of the reactants was $ZrCl_4$: H_2BDC : DMF = 1 : 1 : 135. The typical synthesis procedure was as follows: $ZrCl_4$ (2.33 g, 10 mmol) was dissolved in 55 mL of DMF and terephthalic acid (1.66 g, 10 mmol) in 50 mL of DMF. The ligand solution was slowly added to the metal salt solution and after 30 min of stirring, the mixture was distributed into three appropriately sized Teflon-lined autoclaves. The autoclaves were placed in an oven at 120 °C for 24 h. The precipitates were collected *via* centrifugation, thoroughly washed with DMF (20 mL twice) and then immersed in 20 mL of methanol for 3 days. After separation, the solid products were dried in an oven at 65 °C overnight and then in a vacuum oven (5×10^{-2} mbar) at 150 °C for 12 h. The combined yield was 1.88 g (68%).

Preparation of LiCl@UiO-66 CSPM samples

Three different concentrations of LiCl solution, 5.9 mol L^{-1}, 10.1 mol L^{-1} and 15.5 mol L^{-1}, were prepared. UiO-66 samples were outgassed at 150 °C under vacuum (5×10^{-2} mbar) to remove water and volatile impurities. Activated UiO-66 (500 mg) was immersed in 10 mL of LiCl solution with different concentrations for 4 hours at room temperature. The solid samples were separated from the LiCl solution by centrifugation and decantation of the supernatant, and then washed one time with 8 mL of water for 5 minutes to remove any salt adhering to the outside surface of the MOF particles (Scheme S1, ESI†). Finally, the samples were dried at 65 °C in an oven overnight. Yields were 515 mg, 550 mg and 587 mg, for LiCl@UiO-66_*x*, *x* = 9, 19, 30, respectively. For impregnation, the times of 12 h (ref. 22 and 31) and of 2 h or less[30,35] were reported in the literature. We have conducted the impregnation procedure for 6 or 4 hours with different concentrations of LiCl, which led to similar results. Thus, we decided to choose the less time-consuming procedure.

The composite LiCl@UiO-66_36 was obtained from UiO-66 impregnated with the 15.5 mol L^{-1} LiCl solution under the same conditions, except that the time for the washing process was only 2 minutes.

For the recycled UiO-66 from LiCl@UiO-66_30, samples of 50 mg each were immersed in 10 mL of methanol under stirring for 12 h, and then separated by centrifugation. The samples were dried and kept at 65 °C until analyzed further.

Results and discussion

Synthesis

Lithium chloride was used because of its large availability, low cost and excellent water vapor uptake capacity. Three UiO-66-based CSPMs were synthesized by immersion of activated UiO-66 (outgassed at 150 °C for 16 h under vacuum) in an aqueous solution (10 mL) of LiCl with different concentrations (5.9 mol L^{-1}, 10.1 mol L^{-1} and 15.5 mol L^{-1}) for 4 hours at room temperature (see the Exp. section for details). We used a salt solution whose volume (V_s) exceeded the pore volume of UiO-66

Table 1 LiCl content in UiO-66-based CSPMs

Composite[a]	Theor. max[b] wt% LiCl	wt% LiCl content[c] by AAS	wt% LiCl content[c] by ICP-OES	Atomic ratio Li : Zr[d]
LiCl@UiO-66_9	83	9	10	0.88
LiCl@UiO-66_19	89	19	20	1.53
LiCl@UiO-66_30	93	30	29	2.80

[a] The suffix _*x* in LiCl@UiO-66_*x* indicates wt% LiCl = $m_{LiCl}/m_{CSPM} \times 100\%$ in the composite and was derived from postsynthetic AAS measurement. [b] The theoretical maximum wt% LiCl if the full amount of LiCl would have been impregnated into the MOF. [c] LiCl content calculated from postsynthetic Li determination by AAS or ICP-OES; standard deviation of wt% LiCl is ±1. [d] The atomic ratio of Li : Zr was measured by ICP-OES.

(V_p, that is, $V_s > V_p$). This method is called wet impregnation.[28] If the volume of the salt solution would have been the same as the pore volume (*i.e.* $V_s = V_p$) then this method is termed dry impregnation or incipient wetness impregnation.[28]

By mass, the offered amounts of LiCl were 2.5 g, 4.2 g and 6.7 g per 0.5 g of MOF. The samples were collected after centrifugation and washed to remove the inorganic salt adhering at the outside of the UiO-66 matrix. From atomic absorption spectroscopy (AAS) the mass fraction of LiCl in the CSPM samples was determined to be 9, 19 and 30 wt% (see details in the ESI†). The samples were abbreviated accordingly as LiCl@UiO-66_*x*, where *x* is the mass fraction $m_{LiCl}/m_{CSPM} \times 100\%$ of LiCl in the composite (Table 1). The wt% of both Li and Zr was measured by inductively coupled plasma – optical emission spectroscopy (ICP-OES), confirming the above AAS values for wt% LiCl, and yielding the molar ratio of Li to Zr (Table 1). The amount of LiCl in the composite increases, with the increase of impregnation salt concentration (Table 1). Still, from the theoretically possible loading of about 90 wt% of LiCl only about 30 wt% of LiCl was found incorporated (after the washing step).

We emphasize that in our wet impregnation we did not let the excess salt solution dry to prevent salt precipitation on the matrix surface. In our work a specific amount of deionized water was used to remove the excess salt adhered on the external surfaces of the composites. Hence, only part of the salt was inserted into the pores of the material and the rest was removed. It is worth noting that such washing workups are necessary in order to remove free inorganic salt precipitates from the external surfaces of the MOF and to achieve a true salt@MOF incorporation in a composite. Yet such washing is rarely done in the literature following the wet impregnation.[23] Most authors simply allow the solvent from the salt solution to dry without separation by decantation or washing.[30,31] This then yields rather a physical mixture of the salt and MOF with only part of the salt incorporated into the MOF. In comparison to other wet impregnation studies with a similar separation (and washing) workup, the salt content of the LiCl@UiO composite presented here is similar to the achieved salt incorporation in other studies.[36,37] For example, for lithium chloride in silica gel the LiCl content in the composite was 13 wt% when the lithium chloride solution was 30 wt%.[36] When impregnating calcium chloride in silica gel the $CaCl_2$ content in the composite was between 12 and 35 wt% for $CaCl_2$ offered up to the solubility limit in water.[37] We have to emphasize again that for salt@MOF similar separation (and washing) workups are very seldom carried out after wet impregnation. Other authors use wet impregnation without including a separation step of the supernatant excess salt solution and allow the salt solution to dry with salt precipitation on the matrix surface. Then higher weight percentages of salt@MOF became possible, such as 60 wt% $CaCl_2$ or 42 wt% LiCl in MIL-101(Cr).[31]

Powder X-ray diffractograms (PXRDs) of UiO-66 and CSPMs show that the structure of UiO-66 is preserved after the wet impregnation with LiCl solution (Fig. 1). Reflections corresponding to anhydrous or hydrated LiCl are not clearly observed in the PXRD pattern of the CSPM samples, although

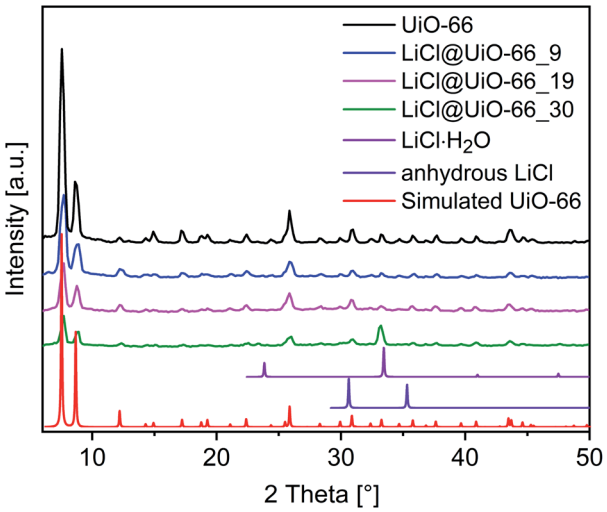

Fig. 1 PXRD patterns of UiO-66, LiCl@UiO-66_*x*, *x* = 9, 19, 30, anhydrous LiCl (COD number: 1011314), $LiCl \cdot H_2O$ (COD number: 101495) and simulated diffractogram of UiO-66 (CCDC number: 1018045).[40]

there may be an overlap with the nearby UiO reflections in the 2θ region of 30–36°. Still the near absence of the characteristic peak at 24° 2θ for $LiCl \cdot H_2O$ rules out a significant $LiCl \cdot H_2O$ crystallization on the outer MOF surface. Inside the MOF, the pores are too small to allow for the formation of a diffracting crystalline LiCl phase, that is, with several unit cells in each direction. For the three CSPM samples, a significant decrease of the relative intensity of the diffraction Bragg peaks was observed with increasing LiCl content and in comparison to neat UiO-66 (under identical measurement conditions). This decrease is caused by the inorganic salt inside the matrix. We use approximately the same mass amount of the probes in our given sample holders. As the relative amount of MOF decreases in the composite with a higher (non-diffracting) salt content, there will be a smaller amount of MOF on the sample holder. With the incorporation of guest species in the pores of MOFs, also the electron density changes can lead to the

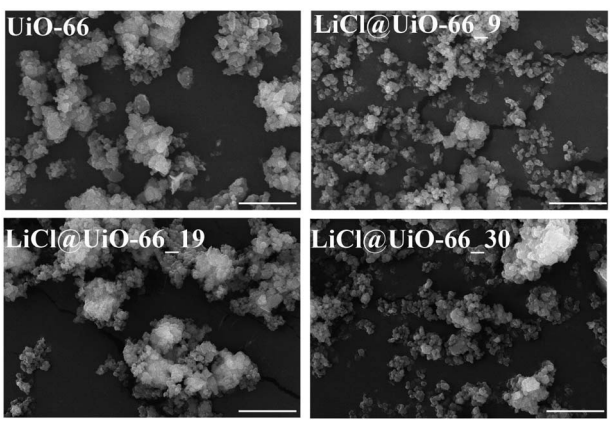

Fig. 2 SEM images of UiO-66 and LiCl@UiO-66_*x*, *x* = 9, 19, 30. Scale bar 5 μm.

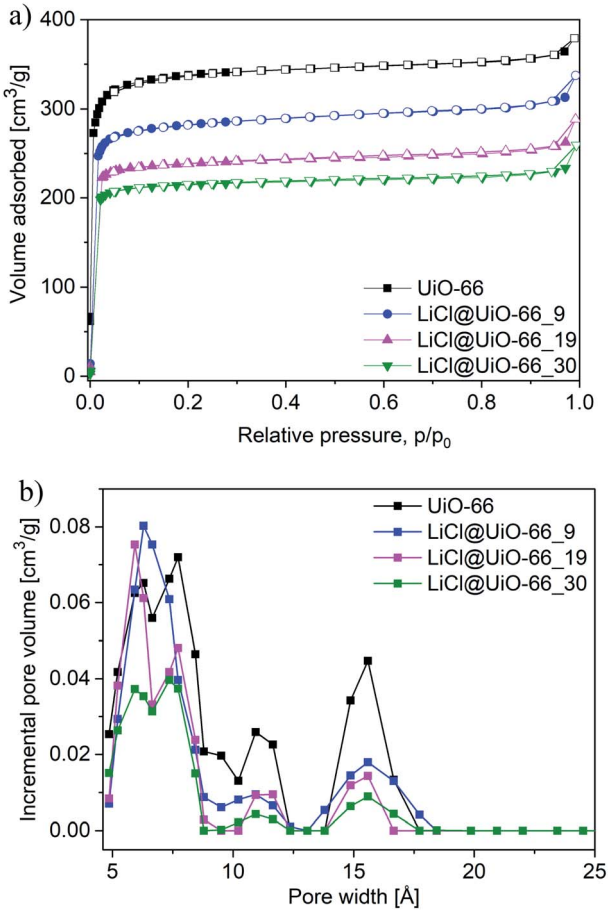

Fig. 3 (a) N_2 sorption isotherms of UiO-66 and LiCl@UiO-66_x (x = 9, 19, 30). Filled symbols, adsorption; empty symbols, desorption. (b) Pore size distribution of UiO-66 and LiCl@UiO-66_x. Pore size distributions were derived using the NLDFT method at 77 K.

decrease of PXRD intensity, especially in the low-angle range.[30,38,39] Scanning electron microscopy (SEM) images show that UiO-66 is crystallized as intergrown nano-sized particles. Under higher magnification, round 200 nm-sized particles could be observed. The SEM images of UiO-66 and its CSPMs show retention of the crystallite morphology (Fig. 2). This also supports the absence of LiCl having formed outside the UiO-66 particles.

Lithium cannot be detected by using an energy dispersive X-ray (EDX) detector because as a light element it has a low X-ray (emission) yield due to the competing and predominant Auger electron emission.[41] The co-existence of Zr and Cl in the CSPM samples was confirmed by SEM-EDX elemental mapping (Fig. S3, ESI†) and demonstrates that LiCl was homogeneously distributed.

UiO-66 and other Zr-MOFs are known for, and are prone to, missing-linker defects.[42] Zirconium-based MOFs can tolerate a detectable and significant defect amount without losing their structural stabilities.[43] The calculation of linker defects was carried out by the quantitative analysis of thermogravimetric analysis (TGA) data (Fig. S4, ESI†), followed by the determination of linker defects by Shearer.[42] From TGA the number of missing-linker defects of UiO-66 was derived as 1.4 and the corresponding simplified formula unit then should be $[Zr_6O_{7.4}(BDC)_{4.6}]$ (compared to $[Zr_6O_6(BDC)_6]$).

Nitrogen physisorption measurements on neat UiO-66 and CSPMs exhibit Type I isotherms, which are indicative of microporous materials.[44] As shown in Fig. 3a, the nitrogen adsorption and desorption isotherms showed almost no hysteresis. The Brunauer–Emmett–Teller (BET) surface area, and total and micropore volume in the CSPMs exhibited a significant decrease, compared to neat UiO-66 (Table 2). This is attributed to the fact that the micropores of UiO-66 are filled with the incorporated LiCl. This pore filling by LiCl in an otherwise unchanged UiO-66 structure was verified through the removal of LiCl and the re-establishing of the original porosity. To remove LiCl, LiCl@UiO-66_30 was immersed in methanol for 12 h at room temperature (see the Exp. section for details). The regained UiO-66 had a BET surface area of 1324 $m^2\ g^{-1}$ and a total pore volume of 0.53 $cm^3\ g^{-1}$, which is similar to pristine UiO-66 (1360 $m^2\ g^{-1}$ and 0.55 $cm^3\ g^{-1}$) (Table 2). The PXRD of the regained UiO-66 from LiCl@UiO-66_30 exhibits similar peak intensities to pristine UiO-66 under identical measurement conditions and, thereby, confirmed the interpretation of decreasing peak intensity being due to the LiCl content (Fig. S5, ESI†).

The neat UiO-66 framework features pores of 8 and 11 Å (Fig. 3b), which are attributed to the tetrahedral and octahedral cages,[45,46] with the cages connected by triangular windows with an aperture width of 6 Å. The pore diameter range between ~14 and 18 Å is due to missing cluster (reo-type) defects.[47–49] CSPMs exhibit similar pore size distributions to UiO-66; however, the pores with 6 and 8 Å width are slightly shifted to smaller diameters, while the relative number of pores centered at 11 and 16 Å of UiO-66 decreased with the increase of impregnated salt in the CSPMs.

Table 2 Porosity characteristics of neat UiO-66 and LiCl@UiO-66_x, x = 9, 19, 30

	S_{BET}[a] [$m^2\ g^{-1}$]	V_{total}[b] [$cm^3\ g^{-1}$]	V_{micro}[c] [$cm^3\ g^{-1}$]	V_{micro}/V_{total}
UiO-66	1360	0.55	0.42	0.76
LiCl@UiO-66_9	1148	0.47	0.37	0.79
LiCl@UiO-66_19	966	0.39	0.31	0.79
LiCl@UiO-66_30	874	0.35	0.28	0.80
Recycled UiO-66 from LiCl@UiO-66_30	1324	0.55	0.43	0.78

[a] Brunauer–Emmett–Teller (BET) surface areas S_{BET} were obtained from five adsorption points in the pressure range p/p_0 = 0.01–0.05. [b] Total pore volume V_{total} calculated from the N_2 sorption isotherm at 77 K (p/p_0 = 0.90) for pores ≤20 nm diameter. [c] Micropore volume obtained using the t-plot method from five adsorption points in the pressure range p/p_0 = 0.05–0.18.

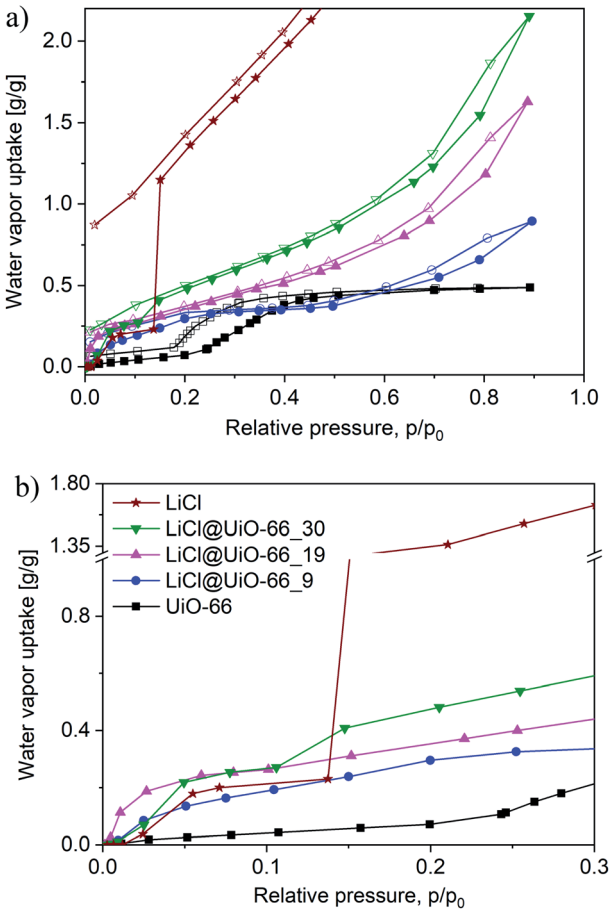

Fig. 4 (a) Water sorption isotherms of neat LiCl, UiO-66 and LiCl@UiO-66_*x*, *x* = 9, 19, 30. Closed and open symbols refer to adsorption and desorption. The LiCl water uptake extends up to 5.46 g g^{-1} (Fig. S6, ESI†). (b) Expanded uptake for clarity in the range of $0 < p/p_0 < 0.30$. From repeated and reproducible volumetric water vapor sorption isotherms the variance of the water uptake values is around 5%.

Water sorption properties

Water vapor sorption isotherms of neat UiO-66, the pure LiCl salt and the three CSPMs were volumetrically measured to examine the effect of the incorporated inorganic salt (Fig. 4a).

The isotherm of UiO-66 shows an S shape curve (Type V isotherm).[44] The three CSPMs mainly exhibit an already increased water uptake over UiO-66 in the low-pressure region, in line with the first uptake step of LiCl at 0.05 p/p_0. The isotherm of the bulk salt shows the step-wise formation of lithium chloride hydrates. This first uptake step of LiCl of 0.21 g g^{-1} below 0.1 p/p_0 can be ascribed to the formation of $LiCl \cdot 0.5H_2O$. The large uptake jump for LiCl at ~0.15 p/p_0 or the second uptake step leading to about 1.25 g of H_2O/g(LiCl) is due to the formation of $LiCl \cdot 3H_2O$ hydrate. LiCl@UiO-66_30 also displays a second step related to the hydration of LiCl. It is worth noting that LiCl@UiO-66_19 and _30 surpass and LiCl@UiO-66_9 matches LiCl in water uptake up to ~0.14 p/p_0 (Table 3, values at $p/p_0 = 0.1$). This is remarkable in view of their lower LiCl content and the only very small uptake contribution from UiO-66.

Concerning the relative uptake pressure, a higher water uptake at low relative pressure over neat LiCl may be viewed as a disadvantage for low-temperature regeneration. However, regeneration is never to be seen as an isolated process, since what matters is the exchanged amount of water per cycle. In general, it is correct that, in absolute terms, an uptake at a relative pressure as low as possible at a given desorption temperature is favorable. However, when it comes to the application, the water exchange per cycle becomes more important.

If the water uptake of the three composites at $p/p_0 = 0.1$ (deducting the UiO contribution) is related to their LiCl wt%, we have 156/0.09, 228/0.19 and 235/0.30 mg(H_2O)/g(LiCl). This translates into a hydration state of $LiCl \cdot 4H_2O$ for LiCl@UiO-66_9, $LiCl \cdot 3H_2O$ for LiCl@UiO-66_19 and $LiCl \cdot 2H_2O$ for LiCl@UiO-66_30 at $p/p_0 = 0.1$ which is much higher than that for neat LiCl. This increased hydration is traced to the nano-dispersion of LiCl in the MOF matrix in connection with the surface energy of these LiCl nanoclusters. The smaller nano-clusters in LiCl@UiO-66_9 will have a higher surface energy and thereby adsorb relatively more water on a mg(H_2O)/g(LiCl) basis at low p/p_0 values. These data are not to be confused with the data in Table 3 which are on a mg(H_2O)/g(CSPM) for LiCl@UiO-66_*x*. Hence, it can be concluded that the properties of a "salt" in a porous matrix vary from those of the neat or bulk salt, due to the interactions between the salt and the matrix, the dispersion of a small particle size and its hydration behavior from the higher salt cluster-surface energy.[50]

The CSPMs LiCl@UiO-66_19 and _30 continue to steadily adsorb water in a Type III isotherm branch above 0.2 p/p_0 again in line with the continuing strong increase in water uptake for LiCl

Table 3 Water vapor uptake for neat and CSPMs at specific relative pressures

	Volumetric water uptake[a,b] [mg g^{-1}] at p/p_0 =			
	0.1	0.3	0.9	Gravimetric water uptake[a] [mg g^{-1}] (at $p/p_0 = 0.9$)
UiO-66	36	179	393	384
LiCl	216	1646	5460	—
LiCl@UiO-66_9	192	338	894	887
LiCl@UiO-66_19	264	455	1628	1682
LiCl@UiO-66_30	271	595	2153	2191

[a] The data mean mg(H_2O)/g(CSPM) for LiCl@UiO-66_*x*. [b] From repeated and reproducible volumetric water vapor sorption isotherms the variance of the water uptake values is around 5%.

after the second step. For LiCl@UiO-66_9 the water uptake reaches a plateau between 0.25 < p/p_0 < 0.45 and the increase in uptake is assumed above 0.5 p/p_0. Evidently, the water uptake of UiO-66-based CSPMs is greatly enhanced over the whole relative pressure (p/p_0) range in comparison with neat UiO-66, demonstrating that LiCl is very effective in increasing the water uptake. In addition, it is known that the inorganic salts could be deposited on the external surface area of the matrix after the pores were completely filled. We have also prepared samples with a higher than 30 wt% amount of LiCl in the CSPM composites LiCl@UiO-66_36 (see the Exp. section for details). However, this sample showed the deliquescence phenomenon after water sorption measurement, which is not desirable for AHT applications. Hence, we did not include a detailed analysis of these samples in the present work. Our samples with up to ~30 wt% amount of LiCl in the CSPM did not show a deliquescence phenomenon even after repeated water sorption measurements, which was supported by the optical microscopy images of LiCl@UiO-66_30 (Fig. S7, ESI†). It could be expected that the pore structure of the metal–organic framework could efficiently prevent the confined inorganic salt from leaching out, due to the limited ability of water uptake to achieve dissolution.

To visualize the water vapor uptake in detail, only the adsorption isotherm parts in the range 0 < p/p_0 < 0.3 were plotted (Fig. 4b). The three LiCl@UiO-66_x (x = 9, 19, 30) CSPMs are more hydrophilic than neat UiO-66 at the initial relative pressure. LiCl@UiO-66_30 assumes the character of pure LiCl and has a slightly weaker uptake of water molecules than LiCl@UiO-66_19 in the low-pressure region up to p/p_0 < 0.05. This may be due to a faster uptake in the less congested pores of LiCl@UiO-66_19 while the higher loaded LiCl@UiO-66_30 would need more time to reach the equilibrium pore filling especially at low pressure. The thermodynamic equilibrium is not necessarily reached in the volumetric adsorption measurement if the set pressure difference criteria (albeit set to the lowest possible value) advance the measurement to the next data point. Above p/p_0 = 0.15 the higher amount of LiCl incorporated in the micropores of UiO-66 also leads to an increased water vapor uptake. The water amounts adsorbed at p/p_0 = 0.3 reached 0.34 g g^{-1}, 0.45 g g^{-1}, and 0.60 g g^{-1}, respectively, which is much higher than that for neat UiO-66 (0.18 g g^{-1}) (Table 3 and Fig. 5). Remarkably the LiCl incorporation increases the water uptake capacity of UiO-66 from 0.18 to 0.60 at p/p_0 = 0.3. The water vapor uptakes measured volumetrically for UiO-66 and the three LiCl@UiO-66_x composites are consistent with the results from the gravimetric measurement (at 0.9 p/p_0, Table 3).

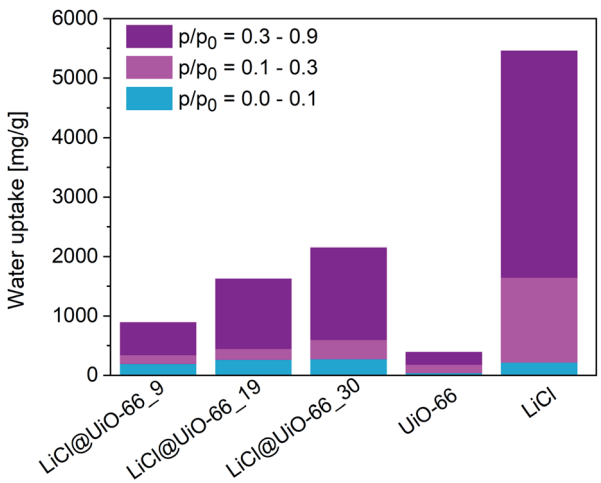

Fig. 5 The water capacity of neat UiO-66, pure LiCl and the three composites LiCl@UiO-66_x (x = 9, 19, 30). From repeated and reproducible volumetric water vapor sorption isotherms the variance of the water uptake values is around 5%.

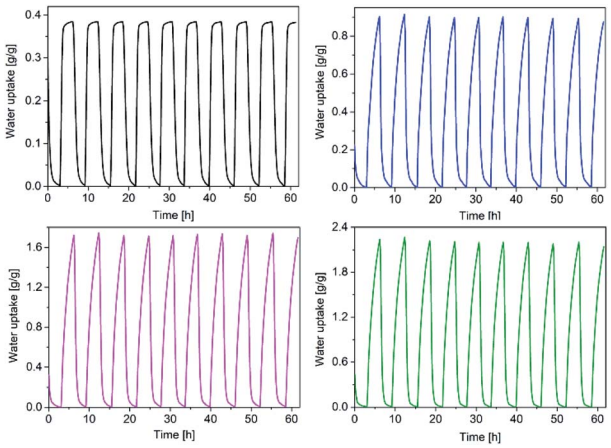

Fig. 6 Gravimetric adsorption and desorption cycles of UiO-66 (black) and the CSPMs LiCl@UiO-66_x, x = 9 (blue), 19 (pink), 30 (green). The gravimetric multi-cycle tests were carried out between relative humidity levels of 90% and 0% under a maximum equilibration time of 3 hours.

In order to evaluate the cycling stability of the CSPMs, the samples were tested gravimetrically by alternatingly exposing the samples to a relative humidity of 90% and 0% (Fig. 6). Like UiO-66, none of the LiCl@UiO-66_x CSPMs shows a visible loss in water uptake. The deviation is −3%, −1% and −4% only (for x = 9, 19, 30, respectively) after 10 adsorption–desorption cycles compared to the first cycle, which is still within the experimental error and the variation seen over the 10 cycles. More cycling experiments were performed under a relative humidity of 80% and 20% (Fig. S8, ESI†) to confirm the stability in practical engineering applications, as a relative humidity of 0% is hardly achieved in a practical device. Over 40 cycles only a slight fluctuation around the equilibrium uptake was observed, which is within the experimental error and caused by the balance drift, but there was no decrease in uptake. In conclusion, the CSPM materials can be viewed as stable towards cyclic water adsorption and desorption within the test procedure and should also be stable under application related conditions. Thus, the superior stability and higher uptake capacity of UiO-66-based CSPMs provides a practical value towards adsorption heat pump applications.

Kinetic study

While for adsorption heat pump applications the specific vapor uptake is of primary importance, adsorption kinetics has also to

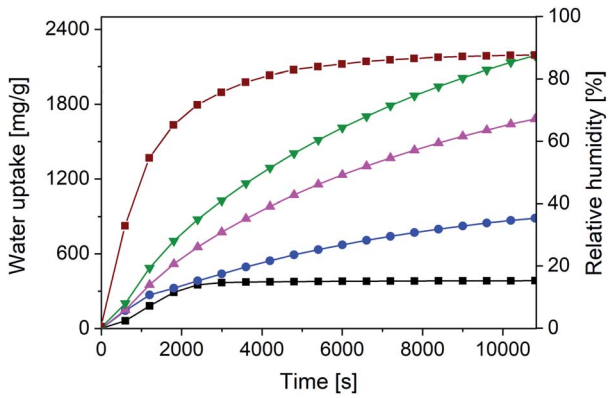

Fig. 7 Gravimetric water sorption measurements of UiO-66 (black) and the CSPMs LiCl@UiO-66_*x*, *x* = 9 (blue), 19 (pink), 30 (green) at 20 °C in comparison to the kinetics curve to reach a set target relative humidity of 90% in the chamber (wine red).

be taken into consideration and is often overlooked. Fig. 7 shows that the dynamic water sorption of uptake over time has a short induction period of ~500 s, followed by a fast uptake section and a slow-down as the amount of adsorbed water vapor gradually reaches saturation. The induction period can be best seen for the pristine MOF and the two _19 and _30 composites in the range from 0 to ~500 seconds. The slope in this time period is not as steep as that of the curves between ~500 and ~1500 seconds. The induction period is mainly caused by the still low relative humidity in the device chamber. The increase in the adsorbed water quantity is intimately related to the amount of impregnated salt. The gravimetric water uptake over time of the pristine UiO-66 and three LiCl@UiO-66_*x* composites were fitted well with a pseudo-first order model (eqn (1), Table 4 and Fig. S9, ESI†).

$$q_t = q_e(1 - e^{-kt}) \quad (1)$$

Here, q_e stands for the equilibrium water sorption quantity (mg g^{-1}), q_t stands for the dynamic water sorption quantity (mg g^{-1}), k stands for the rate coefficient (s^{-1}) and t for time (s). It can be seen from Table 4 that the kinetics of water sorption for the host matrix UiO-66 is faster than that for CSPM adsorbents. UiO-66 reaches saturation, that is, the equilibrium water uptake much faster (after about 3000 s) than that of the CSPMs which need over 10 000 s. This is caused by the increased diffusion resistance due to the hygroscopic salt incorporated into the matrix pores.[51] The CSPMs adsorb a larger amount of water vapor compared to UiO-66 due to the added affinity of LiCl. Yet, the number of larger pores which enable a faster diffusion has decreased in the composites (*cf.* Fig. 3b). Therefore, a longer time is required to reach a saturated or equilibrium adsorption amount, which leads to a lower adsorption rate coefficient of the composite salt compared to the pristine material. Similarly, Teo *et al.* showed that the adsorption rate coefficient of 5% Li(Na) incorporated MIL-101(Cr) is slower than that of pristine MIL-101(Cr).[21]

For CSPMs, the adsorption rate coefficient decreased from LiCl@UiO-66_9 with the increasing incorporated amount of LiCl to LiCl@UiO-66_19 and 30, which have a similar rate coefficient. Still, the adsorption rate coefficient of CSPMs in this work is higher than for silica gel impregnated with LiCl, LiBr and $CaCl_2$, where k ranges from 9.03×10^{-5} s^{-1} to 1.49×10^{-4} s^{-1}.[52] From eqn (1), the calculated equilibrium (saturation) water sorption quantity q_e (for an infinite time at 90% rel. humidity) for pristine UiO-66 and the three CSPMs is 390 mg g^{-1}, 985 mg g^{-1}, 2056 mg g^{-1} and 2619 mg g^{-1} (Table 4). For neat UiO-66 this q_e value compares well with the volumetric water uptake of 393 mg g^{-1} at $p/p_0 = 0.9$ (Table 3) but q_e is increasingly higher than the volumetric water uptake at $p/p_0 = 0.9$ with a higher salt content. For LiCl@UiO-66_30 q_e is 2619 mg g^{-1} while the volumetric water uptake at $p/p_0 = 0.9$ was only 2153 mg g^{-1} (Table 3). This can indicate that the volumetric uptake was not in full equilibrium. For very slow uptakes with decreasingly small pressure differences over time, the set measurement boundary conditions will advance the automatic sorption analyzer to the next data point before full equilibrium was reached.

Table 4 Kinetic parameters from gravimetric water sorption over time[a]

	q_e (mg g^{-1})	k (1 s^{-1})	R^2
UiO-66	390(8)	$6.7(6) \times 10^{-4}$	0.9620
LiCl@UiO-66_9	985(24)	$2.0(1) \times 10^{-4}$	0.9905
LiCl@UiO-66_19	2056(23)	$1.54(3) \times 10^{-4}$	0.9994
LiCl@UiO-66_30	2619(36)	$1.62(4) \times 10^{-4}$	0.9990

[a] Obtained from fitting the gravimetric measurement with eqn (1) (*cf.* Fig. 7 and S9, ESI). Standard deviations are given in parentheses.

Coefficient of performance (COP)

COP is a commonly adopted indicator of the thermodynamic efficiency of the cycling process and depends strongly on the operating conditions. COP is determined as useful energy output divided by the required energy as input,[1] which for the heating model (COP_H) is given by eqn (2) with heat from condensation (Q_{cond}) and heat of adsorption (Q_{ads}).

$$COP_H = \frac{-(Q_{con} + Q_{ads})}{Q_{regen}} \quad (2)$$

The COP_H values can range from 1 to 2.[1] The higher the COP_H values, the better the energetic efficiency for the heating mode. The volumetric adsorption data were fitted using with the Dubinin–Astakhov approach, which is quite common for water@zeolite-systems.[36,37,53] As conditions for a heat pump an evaporator (cold) temperature of 10 °C, a heating or adsorption temperature of 40 °C and a driving (desorption) temperature of 90 °C were used. This leads to a COP_H of 1.64 for LiCl@UiO-66_30 (see details, in the ESI†).

In other work, the coefficient of performance (given in parentheses) for CAU-10 (1.15–1.3) and SAPO-34 (1.35–1.6) at desorption temperatures ranging from 80–120 °C was lower than 1.64, and only MIL-160 showed a slightly higher COP value of 1.67 than LiCl@UiO-66_30 (1.64) when a desorption

Table 5 Coefficients of performance (COP_H) for comparative materials

Compound	Adsorbate	Working conditions, °C ($T_{evap.}/T_{ads.}/T_{des.}$)	COP_H	Ref.
LiCl@UiO-66_30	Water	10/40/90	1.64	This work
CAU-10	Water	15/45/80–120	1.15–1.3	54
SAPO-34	Water	15/45/80–120	1.35–1.6	54
MIL-160	Water	15/45/80–120	1.2–1.67	54
MOF-801(Zr)	Water	15/45/80–120	1–1.58	1
Benchmark AQSOA-Z02	Water	15/45/80–120	1.35–1.6	1
MIL-53(Cr)	Methanol	15/45/80–120	1–1.52	1
$Zn(BDC)(DABCO)_{0.5}$	Methanol	15/45/80–120	1–1.55	1
Activated carbon	Methanol	15/45/80–120	1–1.51	1
MIL-101	Methanol	−23/50/140–190	1–1.21	55
Silica/LiBr	Methanol	−23/50/140–190	1–1.11	55
CAU-3	Ethanol	−23/50/140–180	1–1.07	55
Maxsorb III	Ethanol	−23/50/140–180	1–1.11	55
AX-21(active carbon)	Ammonia	−23/50/140–190	1–1.18	55
SWS-1S[a]	Water	7/55/100–135	1.1–1.4	56
SWS-2L(57)[b]	Water	7/55/125–150	1.2–1.65	56

[a] SWS-1S refers to a silica gel with an average pore radius of 1.8 nm filled with 21.7% $CaCl_2$. [b] SWS-2L(57) refers to a silica gel with an average pore radius of 7.5 nm filled with 57% LiBr.

temperature higher than 100 °C was applied (Table 5).[54] Also, the COP value was lower for MOF-801(Zr) (1–1.58) and benchmark AQSOA-Z02 (1.35–1.6) with water as the working pair, and MIL-53(Cr) (1–1.52), $Zn(BDC)(DABCO)_{0.5}$ (1–1.55) and activated carbon (1–1.51) with methanol as the working pair at desorption temperatures ranging from 80–120 °C.[1] For the adsorbent–adsorbate pairs such as MIL-101-methanol, SG/LiBr-methanol, CAU-3-ethanol, Maxsorb III-ethanol, and AX-21-ammonia, the COP_H ranged only from 1.0 to 1.2.[55] For salt@silica gel SWS composites, the COP value for SWS-1S (1.1–1.4) was lower than 1.64, and the highest COP value for SWS-2L(57) (1.2–1.65) was close to that of LiCl@UiO-66_30 (1.64); however, the desorption temperature was in the range of 125–150 °C (Table 5).[56] Thus, LiCl@UiO-66_30 (1.64) is promising because of its high COP value and a relatively low desorption temperature for regeneration.

Thermal battery applications

Adsorption-based thermal batteries (ATBs) have been recently introduced as an alternative storage device to improve the usability of discontinuously supplied low-grade energy for heating and cooling. The process is based on cyclic adsorption and desorption of a working fluid on a porous material (Scheme 1). ATBs make use of heat at different temperature levels such as thermal solar energy or industrial waste heat as the regeneration energy instead of electricity or fossil fuels.[57,58]

Following the work of Garzón-Tovar and co-workers,[29] we chose the working capacity at low relative pressures (p/p_0 = 0–0.1) being desirable to diminish the requirement of a compressor. Thus, the efficiency of a thermal battery is directly proportional to the working capacity at $p/p_0 = 0.1$ (Table 3 and Fig. 5). LiCl@UiO-66_30 has a high-water capacity of 271

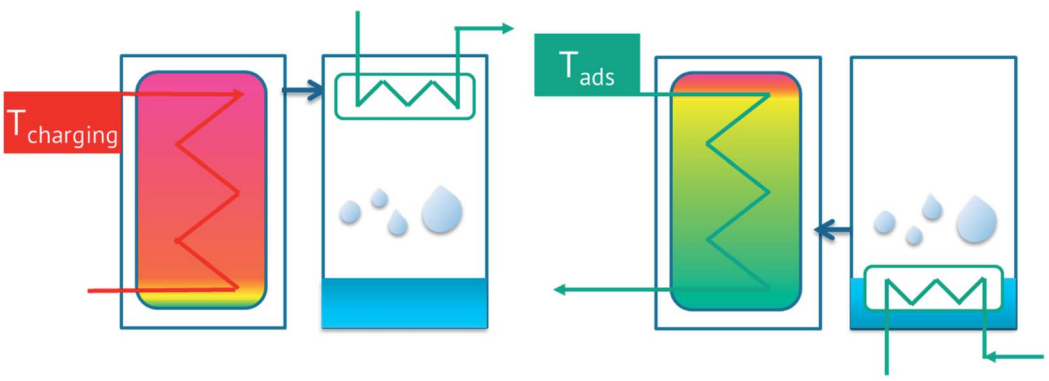

Scheme 1 Schematic working principle of an adsorption-based thermal battery (ATB). To charge the thermal battery (a), heat at a high temperature level has to be applied and the working fluid (*e.g.*, water) has to be collected in a storage using a condenser. The battery can then be discharged (b) by evaporating the working fluid leading to its adsorption. Therefore the ATB can be used for heating by making use of the heat of adsorption as well as for cooling by using the heat of evaporation drawn from the environment.

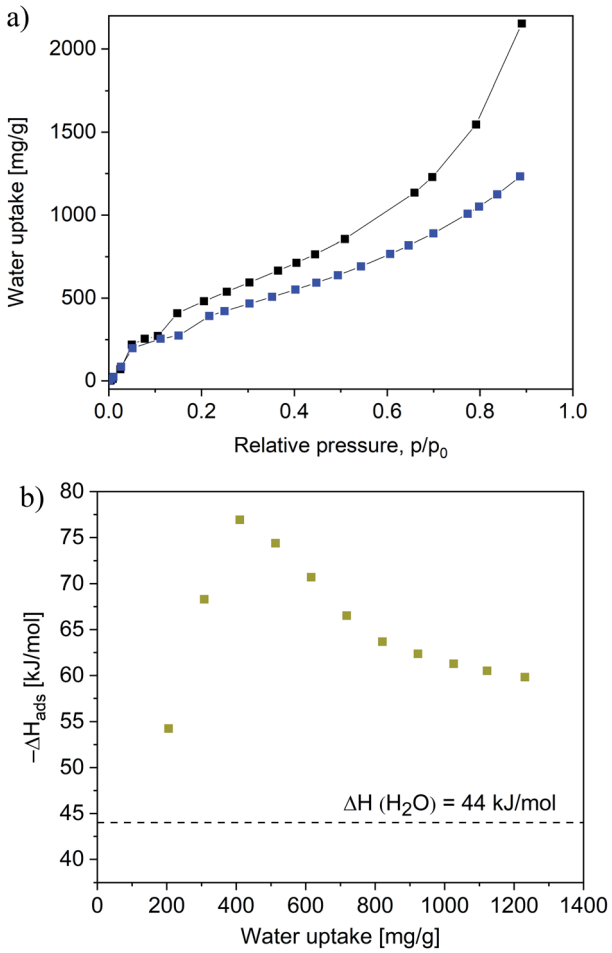

Fig. 8 (a) Water sorption isotherms of LiCl@UiO-66_30 at 293 K (black) and 303 K (blue). (b) Isosteric enthalpy of adsorption for water at LiCl@UiO-66_30. Straight dashed line is the enthalpy of evaporation of water (44 kJ mol^{-1}) at 298 K.

mg g^{-1} at $p/p_0 = 0.1$. The isosteric enthalpy of adsorption for water at LiCl@UiO-66_30 was calculated using water sorption isotherms (Fig. 8a) from two different temperatures (293 K and 303 K) by applying the Clausius–Clapeyron equation (eqn (3)). The enthalpy of adsorption rises initially, goes through a maximum at a water uptake of 0.4 g g^{-1}, which coincides with the inflection point in the second uptake step in the volumetric adsorption isotherm (Fig. 4b and 8a) and then declines gradually with increasing water loading (Fig. 8b). It was found that $-\Delta H_{ads}$ for a working capacity (Δw) of 271 mg g^{-1} (at $p/p_0 = 0.1$) was about 60 kJ mol^{-1}. The heat storage capacity (C_{HS}) was estimated according to eqn (4).

$$\Delta H_{ads} = -R \times \ln\left(\frac{P_2}{P_1}\right) \frac{T_1 \times T_2}{T_2 - T_1} \quad (3)$$

$$C_{HS} = \frac{\Delta H_{ads} \times \Delta\omega}{M_W} \quad (4)$$

where M_w is the molecular mass of water. The heat storage capacity (C_{HS}) for LiCl@UiO-66_30 was calculated to be 900 kJ kg^{-1} (=0.25 kW h kg^{-1}), which outperforms $CaCl_2$@UiO-66_38 with a C_{HS} value of 367 kJ kg^{-1}.[29] According to the U.S. Department of Energy (DOE),[59] the minimum heat storage capacity for ATBs should be 2.5 kW h with the condition of the maximum weight of the heat exchanger system of 35 kg. To achieve the targeted minimum heat storage capacity, only 10 kg of LiCl@UiO-66_30 would be needed. This makes LiCl@UiO-66_30 a promising candidate applicable in adsorption-based thermal batteries.

Conclusions

MOF-based composites of a 'salt inside porous matrix' with LiCl@UiO-66 were fabricated by a facile post-modification wet-impregnation method. Thorough characterization by AAS, ICP-OES, PXRD, N_2 sorption with BET analysis and SEM/EDX in comparison to neat UiO-66 confirms the incorporation of LiCl inside the MOF. Not only the water uptake capacity of LiCl@UiO-66 significantly increased over neat UiO-66, but an analysis of the water vapor sorption isotherms also shows at $p/p_0 = 0.1$ a hydration state of LiCl inside the MOF which is much higher than for neat LiCl. This is traced to the dispersion of small LiCl clusters with their high surface energy in the porous matrix. A kinetic analysis of the water uptake from a gravimetric measurement over time reveals the expected slower adsorption in LiCl@UiO-66 over neat UiO-66 due to pore blocking effects. More importantly, this kinetic analysis also suggests that the volumetric water sorption measurements have not reached full equilibrium, lacking for example an uptake of over 400 mg g^{-1} for LiCl@UiO-66_30 at $p/p_0 = 0.9$ due to instrument artefacts. The high-water adsorption amount of LiCl@UiO-66_30 of 271 mg g^{-1} at $p/p_0 = 0.1$ coincides with a heat storage capacity of 900 kJ kg^{-1}, which makes this hydrothermally stable composite readily applicable in thermal batteries and adsorption heat pumps. As a vision for future work, we believe that a matrix with a larger pore size could increase not only the loading of inorganic salts but also the uptake kinetics. Under the premise of ensuring no deliquescence, we plan to test whether the optimal loading of inorganic salts inside a matrix possessing a larger pore size could then yield a better performance in practical applications.

Conflicts of interest

There are no conflicts to declare.

Acknowledgements

The authors thank Dr Jun Liang for helpful discussion. We thank the China Scholarship Council (CSC) for funding a PhD fellowship to Y. Y. S.

References

1 M. F. de Lange, K. J. Verouden, T. J. Vlugt, J. Gascon and F. Kapteijn, *Chem. Rev.*, 2015, **115**, 12205–12250.
2 E. Hastürk, S.-J. Ernst and C. Janiak, *Curr. Opin. Chem. Eng.*, 2019, **24**, 26–36.

3 F. Jeremias, D. Fröhlich, C. Janiak and S. K. Henninger, *New J. Chem.*, 2014, **38**, 1846–1852.
4 Y. I. Aristov, *Appl. Therm. Eng.*, 2013, **50**, 1610–1618.
5 K. C. Ng, H. T. Chua, C. Y. Chung, C. H. Loke, T. Kashiwagi, A. Akisawa and B. B. Saha, *Appl. Therm. Eng.*, 2001, **21**, 1631–1642.
6 T. Kawano, M. Kubota, M. S. Onyango, F. Watanabe and H. Matsuda, *Appl. Therm. Eng.*, 2008, **28**, 865–871.
7 M. Kubota, T. Ito, F. Watanabe and H. Matsuda, *Appl. Therm. Eng.*, 2011, **31**, 1495–1498.
8 J.-P. Zhang, A.-X. Zhu, R.-B. Lin, X.-L. Qi and X.-M. Chen, *Adv. Mater.*, 2011, **23**, 1268–1271.
9 A. Ristić, N. Z. Logar, S. K. Henninger and V. Kaučič, *Adv. Funct. Mater.*, 2012, **22**, 1952–1957.
10 A. Krajnc, J. Varlec, M. Mazaj, A. Ristić, N. Z. Logar and G. Mali, *Adv. Energy Mater.*, 2017, **7**, 1601815.
11 S. K. Henninger, F. Jeremias, H. Kummer and C. Janiak, *Eur. J. Inorg. Chem.*, 2012, **2012**, 2625–2634.
12 M. J. Kalmutzki, C. S. Diercks and O. M. Yaghi, *Adv. Mater.*, 2018, **30**, 1704304.
13 S. Kayal, A. Chakraborty and H. W. B. Teo, *Mater. Lett.*, 2018, **221**, 165–167.
14 N. Tannert, S.-J. Ernst, C. Jansen, H.-J. Bart, S. K. Henninger and C. Janiak, *J. Mater. Chem. A*, 2018, **6**, 17706–17712.
15 F. Jeremias, A. Khutia, S. K. Henninger and C. Janiak, *J. Mater. Chem.*, 2012, **22**, 10148–10151.
16 J. Canivet, A. Fateeva, Y. Guo, B. Coasne and D. Farrusseng, *Chem. Soc. Rev.*, 2014, **43**, 5594–5617.
17 D. Lenzen, J. Zhao, S. J. Ernst, M. Wahiduzzaman, A. Ken Inge, D. Frohlich, H. Xu, H. J. Bart, C. Janiak, S. Henninger, G. Maurin, X. Zou and N. Stock, *Nat. Commun.*, 2019, **10**, 3025–3034.
18 C. Schlüsener, M. Xhinovci, S.-J. Ernst, A. Schmitz, N. Tannert and C. Janiak, *Chem. Mater.*, 2019, **31**, 4051–4062.
19 N. Ko, P. G. Choi, J. Hong, M. Yeo, S. Sung, K. E. Cordova, H. J. Park, J. K. Yang and J. Kim, *J. Mater. Chem. A*, 2015, **3**, 2057–2064.
20 M. Wickenheisser, F. Jeremias, S. K. Henninger and C. Janiak, *Inorg. Chim. Acta*, 2013, **407**, 145–152.
21 H. W. B. Teo, A. Chakraborty and S. Kayal, *Appl. Therm. Eng.*, 2017, **120**, 453–462.
22 X. Zheng and R. Wang, *Int. J. Refrig.*, 2019, **98**, 452–458.
23 J. Xu, T. Li, J. Chao, S. Wu, T. Yan, W. Li, B. Cao and R. Wang, *Angew. Chem., Int. Ed.*, 2020, **59**, 5202–5210.
24 L. G. Gordeeva and Y. I. Aristov, *Int. J. Low-Carbon Technol.*, 2012, **7**, 288–302.
25 Yu. I. Aristov, An optimal sorbent for adsorption heat pumps: thermodynamic requirements and molecular design, in *Proc. VI Minsk International Seminar 'Heat Pipes, Heat Pumps, Refrigerators', Minsk*, 12–15 September, 2005, pp. 342–353.
26 Yu. I. Aristov, M. M. Tokarev, G. Cacciola and G. Restuccia, *React. Kinet. Catal. Lett.*, 1996, **59**, 325–334.
27 Y. N. Zhang, R. Z. Wang and T. X. Li, *Energy*, 2018, **156**, 240–249.
28 K. Bourikas, C. Kordulis and A. Lycourghiotis, *Catal. Rev.*, 2006, **48**, 363–444.
29 L. Garzón-Tovar, J. Pérez-Carvajal, I. Imaz and D. Maspoch, *Adv. Funct. Mater.*, 2017, **27**, 1606424.
30 A. Permyakova, S. Wang, E. Courbon, F. Nouar, N. Heymans, P. D'Ans, N. Barrier, P. Billemont, G. De Weireld, N. Steunou, M. Frère and C. Serre, *J. Mater. Chem. A*, 2017, **5**, 12889–12898.
31 B. Tan, Y. Luo, X. Liang, S. Wang, X. Gao, Z. Zhang and Y. Fang, *Microporous Mesoporous Mater.*, 2019, **286**, 141–148.
32 K. Leus, T. Bogaerts, J. De Decker, H. Depauw, K. Hendrickx, H. Vrielinck, V. Van Speybroeck and P. Van Der Voort, *Microporous Mesoporous Mater.*, 2016, **226**, 110–116.
33 L. Hu, T. Ge, Y. Jiang and R. Wang, *Int. J. Refrig.*, 2014, **35**, 69–75.
34 J. H. Cavka, S. Jakobsen, U. Olsbye, N. Guillou, C. Lamberti, S. Bordiga and K. P. Lillerud, *J. Am. Chem. Soc.*, 2008, **130**, 13850–13851.
35 B. N. Truong, J. Park, O. K. Kwon and I. Park, *Mater. Lett.*, 2018, **215**, 137–139.
36 L. X. Gong, R. Z. Wang, Z. Z. Xia and C. J. Chen, *J. Chem. Eng. Data*, 2010, **55**, 2920–2923.
37 K. Daou, R. Z. Wang and Z. Z. Xia, *Appl. Therm. Eng.*, 2006, **26**, 56–65.
38 Y. Ban, Z. Li, Y. Li, Y. Peng, H. Jin, W. Jiao, A. Guo, P. Wang, Q. Yang, C. Zhong and W. Yang, *Angew. Chem., Int. Ed.*, 2015, **54**, 15483–15487.
39 G. Férey, C. Mellot-Draznieks, C. Serre, F. Millange, J. Dutour, S. Surblé and I. Margiolaki, *Science*, 2005, **309**, 2040–2042.
40 S. Øien, D. Wragg, H. Reinsch, S. Svelle, S. Bordiga, C. Lamberti and K. P. Lillerud, *Cryst. Growth Des.*, 2014, **14**, 5370–5372.
41 S. Muto and K. Tatsumi, *Microscopy*, 2016, **66**, 39–49.
42 G. C. Shearer, S. Chavan, S. Bordiga, S. Svelle, U. Olsbye and K. P. Lillerud, *Chem. Mater.*, 2016, **28**, 3749–3761.
43 S. Yuan, J. S. Qin, C. T. Lollar and H. C. Zhou, *ACS Cent. Sci.*, 2018, **4**, 440–450.
44 M. Thommes, K. Kaneko, A. V. Neimark, J. P. Olivier, F. Rodriguez-Reinoso, J. Rouquerol and K. S. W. Sing, *Pure Appl. Chem.*, 2015, **87**, 1051–1069.
45 M. Kim and S. M. Cohen, *CrystEngComm*, 2012, **14**, 4096–4104.
46 Q. Yang, A. D. Wiersum, P. L. Llewellyn, V. Guillerm, C. Serre and G. Maurin, *Chem. Commun.*, 2011, **47**, 9603–9605.
47 M. Taddei, *Coord. Chem. Rev.*, 2017, **343**, 1–24.
48 C. A. Clark, K. N. Heck, C. D. Powell and M. S. Wong, *ACS Sustainable Chem. Eng.*, 2019, **7**, 6619–6628.
49 B. Bueken, N. Van Velthoven, A. Krajnc, S. Smolders, F. Taulelle, C. Mellot-Draznieks, G. Mali, T. D. Bennett and D. De Vos, *Chem. Mater.*, 2017, **29**, 10478–10486.
50 F. Kuznik, Energy Storage by Adsorption Technology for Building, in *Handbook of Energy Systems in Green Buildings*, ed. R. Wang and X. Zhai, Springer, Berlin, Heidelberg. 2018, pp. 1025–1051, DOI: 10.1007/978-3-662-49120-1_42.
51 B. Dawoud and Y. Aristov, *Int. J. Heat Mass Transfer*, 2003, **46**, 273–281.
52 X. Zheng, T. S. Ge, R. Z. Wang and L. M. Hu, *Chem. Eng. Sci.*, 2014, **120**, 1–9.

53 S.-J. Ernst, F. Jeremias, H.-J. Bart and S. K. Henninger, *Ind. Eng. Chem. Res.*, 2016, **55**, 13094–13101.
54 A. Cadiau, J. S. Lee, D. Damasceno Borges, P. Fabry, T. Devic, M. T. Wharmby, C. Martineau, D. Foucher, F. Taulelle, C.-H. Jun, Y. K. Hwang, N. Stock, M. F. De Lange, F. Kapteijn, J. Gascon, G. Maurin, J.-S. Chang and C. Serre, *Adv. Mater.*, 2015, **27**, 4775–4780.
55 D. B. Boman, D. C. Hoysall, D. G. Pahinkar, M. J. Ponkala and S. Garimella, *Appl. Therm. Eng.*, 2017, **123**, 422–434.
56 Y. I. Aristov, G. Restuccia, G. Cacciola and V. N. Parmon, *Appl. Therm. Eng.*, 2002, **22**, 191–204.
57 T. X. Li, R. Z. Wang and T. Yan, *Energy*, 2015, **84**, 745–758.
58 I. S. Girnik, A. D. Grekova, T. X. Li, R. Z. Wang, P. Dutta, S. S. Murthy and Y. I. Aristov, *Renewable Sustainable Energy Rev.*, 2020, **123**, 109748.
59 Advanced Research Projects Agency-DOE, *HEATS Program Overview*, https://arpa-e.energy.gov/sites/default/files/documents/files/HEATS_ProgramOverview.pdf, accessed Oct, 2016.